Acta Materialia 288 (2025) 120826

Contents lists available at ScienceDirect

Acta Materialia

journal homepage: www.elsevier.com/locate/actamat

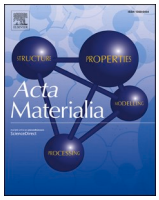

Full length article

Multimodality of critical strength for incipient plasticity in $L1_2$- precipitated $(CoCrNi)_{94}Al_3Ti_3$ medium-entropy alloy: Coherent interface-facilitated dislocation nucleation

Qian Zhang [a,b], Junwei Qiao [a,*], Yakai Zhao [c,*], Jae-il Jang [d], Upadrasta Ramamurty [b,c]

[a] Laboratory of High-Entropy Alloys, College of Materials Science and Engineering, Taiyuan University of Technology, Taiyuan 030024, China
[b] School of Mechanical and Aerospace Engineering, Nanyang Technological University, Singapore 639798, Singapore
[c] Institute of Materials Research and Engineering (IMRE), Agency for Science, Technology and Research (A*STAR), Singapore 138634, Singapore
[d] Division of Materials Science and Engineering, Hanyang University, Seoul 04763, South Korea

ARTICLE INFO

Keywords:
Medium-entropy alloy
Coherent $L1_2$ phase
Nanoindentation
Incipient plasticity
Dislocation nucleation mechanisms

ABSTRACT

The stochastic nature of the incipient plasticity in $(CoCrNi)_{94}Al_3Ti_3$ medium-entropy alloy (MEA) precipitation-hardened by $L1_2$ phase of various sizes is explored systematically by nanoindentation. As the $L1_2$ phase continuously coarsens during aging (with an average radius varying from 3 to 82 nm), the critical strength for incipient plasticity, τ_y, measured with a small radius tip unexpectedly decreases first and then increases, attaining its minimum when the aging time $t = 60$ mins. The distributions of τ_y for all samples are intrinsically multimodal, indicating the co-existence of different dislocation nucleation mechanisms. Specifically, a trimodal distribution is found for the samples in the homogenized state and aged up to 18 mins, whereas the strength distributions in the samples aged for 60 mins and more is bimodal. Considering the size of the stressed volume during the indentation and the inter-spacing between various crystalline defects (dislocations, monovacancies, divacancies, and coherent phase interfaces), the potential deformation mechanisms in all aged samples were ascertained to include monovacancy-induced heterogeneous dislocation nucleation in the matrix near and far from the precipitate/matrix interface, interface-assisted heterogeneous dislocation nucleation, as well as homogeneous dislocation nucleation (only for large $L1_2$ particles). Results suggest that the coherent phase interface can reduce the critical stress for dislocation nucleation and thus can act as a unique generator of dislocations, which depends on the inter-particle spacing and the size of $L1_2$ phase.

1. Introduction

A major drawback, in general, of the monophasic high entropy alloys (HEAs) with the face centered cubic (FCC) crystal structure is their relatively poor strength. Several different alloy design strategies are being employed for overcoming this limitation, precipitation hardening being the most prominent. HEAs with high density of nanoscale precipitates have been shown to achieve ultrahigh strength while maintaining large ductility [1–6]. For example, He *et al.* [7] reported that $(FeCoNiCr)_{94}Ti_2Al_4$ (at.%) HEA reinforced by coherent nanoscale particles with the $L1_2$ crystal structure exhibit a tensile strength of ~1.3 GPa with a tensile elongation of 17 %. In another work [8], alloying with the minor quantities of Al and Ti was demonstrated to enhance the yield and tensile strengths of $L1_2$-strengthened CoCrNi-based medium-entropy alloy (MEA) by ~70 % and ~44 % respectively, while maintaining a ductility of ~45 %. It is suggested that, in addition to serving as obstacles to dislocation motion, the coherent nanoscale $L1_2$ precipitates can also act as generators of mobile dislocations [9]. Compared with the monophasic HEAs, such precipitates will introduce coherent phase interfaces into the crystal lattice. Whether the coherency strains associated with them will lower the activation energy for dislocation nucleation sufficiently is a question that has not been experimentally addressed.

For detecting and understanding the nucleation of dislocations, nanoindentation technology that probes small-scale mechanical behavior [10] and can identify the sub-micron-scale incipient plasticity of the alloy is probably the most appropriate method. When the nanoindentation is performed with an indenter with small tip radius, the elastic to elastoplastic transition can be precisely captured through the

* Corresponding authors.
E-mail addresses: qiaojunwei@gmail.com (J. Qiao), zhao_yakai@imre.a-star.edu.sg (Y. Zhao).

https://doi.org/10.1016/j.actamat.2025.120826
Received 5 November 2024; Received in revised form 26 January 2025; Accepted 12 February 2025
Available online 13 February 2025

load at the first displacement burst (or pop-in) on the load-displacement (*P*-h) curve measured under the load control mode [11–14]. If the alloy is completely annealed, the extremely-small contact radius (usually a few tens of nanometers) between the indenter and the sample when the first pop-in occurs makes the probability of encountering existing dislocations fairly slim [15]. In this case, the incipient plasticity is controlled by the nucleation of dislocations [16–19]. Benefit from the effective mechanical response detection at nanoscale, it is expected to derive the specific role of the coherent phase interface based on the evolution of the critical strength for incipient plasticity and its distribution characteristics.

In general, the critical load, P_I, that causes the first pop-in is statistical in nature, and a detailed analysis of it can be used to understand the nature of the incipient plasticity. In most cases, such strength distribution in conventional metals (or even HEAs) is taken to be unimodal in nature [13,20–24]. This, implicitly, assumes that a single deformation mechanism is responsible for the occurrence of the first pop-in. For example, Zhu *et al.* [21] conducted incipient plasticity tests on CoCrFeMnNi HEA at different temperatures and stated that the vacancy-mediated heterogeneous dislocation nucleation mechanism is predominant. However more than one deformation mechanism may get activated during nanoindentation, which would result in bi- or multi-modal strength distributions. Zhao *et al.* [16,25] reported a bimodal feature in the pop-in stress distribution in CoCrFeNi and CoCrFeMnNi alloys. Their analysis of the experimental data suggests that when the indenter tip radius is sufficiently small, the first pop-in is controlled by monovacancy-assisted heterogeneous dislocation nucleation and/or homogeneous dislocation nucleation. When a large radius tip is used, the deformation mechanisms transition to the activation of pre-existing dislocations and vacancy cluster/grain boundary assisted heterogeneous dislocation nucleation.

For examining the role of coherent interfaces on dislocation nucleation, a small radius tip is preferred. In the stressed zone beneath the indenter, the types and distribution states of defects determine which nucleation mechanism will dictate the incipient plasticity characteristics. Along with the coherent $L1_2$ phase precipitates, the crystallographic defects within the alloy such as vacancies, vacancy clusters, dislocations, coherent phase interfaces and grain boundaries, are all candidates that could influence the measured mechanical response. Amongst them, all the defects except the coherent interface make dislocation nucleation easier compared with that of the homogeneous dislocation nucleation in a perfect lattice [16,26,27]. Whether the coherent interface also exerts a similar influence on the dislocation nucleation is yet to be examined in detail. Keeping the above in view, we employ nanoindentation on a medium entropy alloy (MEA), $(CoCrNi)_{94}Al_3Ti_3$ that was homogenized and then subjected precipitation aging treatment for varying time periods, for a detailed experimental examination of the role of precipitates and the interface between them and the matrix on the incipient plasticity.

2. Materials and experiments

The $(CoCrNi)_{94}Al_3Ti_3$ alloy ingot used in this study was prepared by arc-melting of pure elements (purity $\geq$ 99.9 wt.%) in the required proportion under a high-purity argon atmosphere and then casting the molten alloy into a copper crucible that was water-chilled. To ensure chemical homogeneity, the ingot was flipped and remelted at least four times and then drop-cast into a rectangular plate. Subsequently, the plate was hot rolled at 950 °C with a thickness reduction of 75 %. After grinding the oxide skin off the surface of the hot-rolled sheet, the sample was sealed in a quartz tube filled with high purity argon gas, and then homogenized at 1200 °C for 24 h, followed by water quenching. Finally, the sheet was cut into multiple small samples, and aged at 950 °C for 1, 6, 18, 60, 180, 600, and 6000 mins (the time interval was selected based on Refs. [28,29]). Prior to the nanoindentation experiments, all the samples were mechanically polished and then electropolished in a mixture of 70 % methanol, 20 % glycerol, and 10 % perchloric acid in volume percent (vol.%) to remove any work-hardened surface layer.

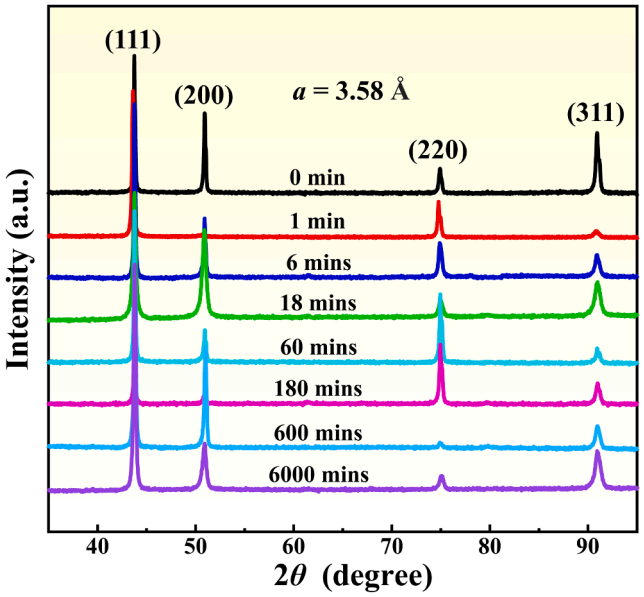

Fig. 1. XRD patterns of $(CoCrNi)_{94}Al_3Ti_3$ alloy in homogenized (0 min) and aged states.

X-ray diffraction (XRD, PANalytical AERIS) with Cu Kα radiation was utilized to investigate the phase(s) and lattice parameters. For the characterization of the coherent $L1_2$ phase in all the aged samples, transmission electron microscopy (TEM) analysis was performed using a FEI Talos F200X microscope operating at 200 kV. TEM samples were firstly mechanically ground to a thickness below 50 μm using SiC paper, then punched into 3 mm diameter discs. They were further thinned using the twin-jet electro-polishing (Struers Tenupol 5) technique in a $HClO_4$:C_2H_6O = 1:9 solution with a voltage of ~15 V at a temperature of about −25 °C.

Nanoindentation tests were performed using the Bruker TI Premier instrument equipped with a Berkovich tip. The tip radius was calibrated on a reference fused quartz sample based on Hertzian theory [30] to be ~434 nm. All the tests were carried out at room temperature and in load-control mode, with a peak load, P_{max}, of 480 μN and loading rate of 60 μN/s. For obtaining large datasets that contain statistically significant data, 10 × 10 grid indentations were performed within three arbitrary grains on the surface of each sample, with a spacing of 5 μm in both horizontal and vertical directions. The grid edges were kept >20 μm away from the grain boundaries to avoid the nucleation of dislocations from them. In total, 290 load-displacement responses (at least) exhibiting clear first pop-in phenomena were obtained on each sample. Naghdi *et al.* [31] demonstrated that when a nanoindentation load is applied and held constant, further reorganization of local chemical ordering may occur within the alloy. This phenomenon was not considered here due to the arduous verification and the potentially negligible impact on the results of this paper. In order to understand the macroscopic mechanical properties, Vickers hardness and indentation plastometry tests were conducted. For Vickers hardness, peak load of 0.3 kgf for a dwell time of 10 s was used. For the indentation plastometry, a commercial machine (Plastometrex PLX-Benchtop) was utilized which conducts spherical indentation test (spherical tip radius: 0.5 mm) and then finite element method (FEM) based on the surfacing profiling results of the indentation [32].

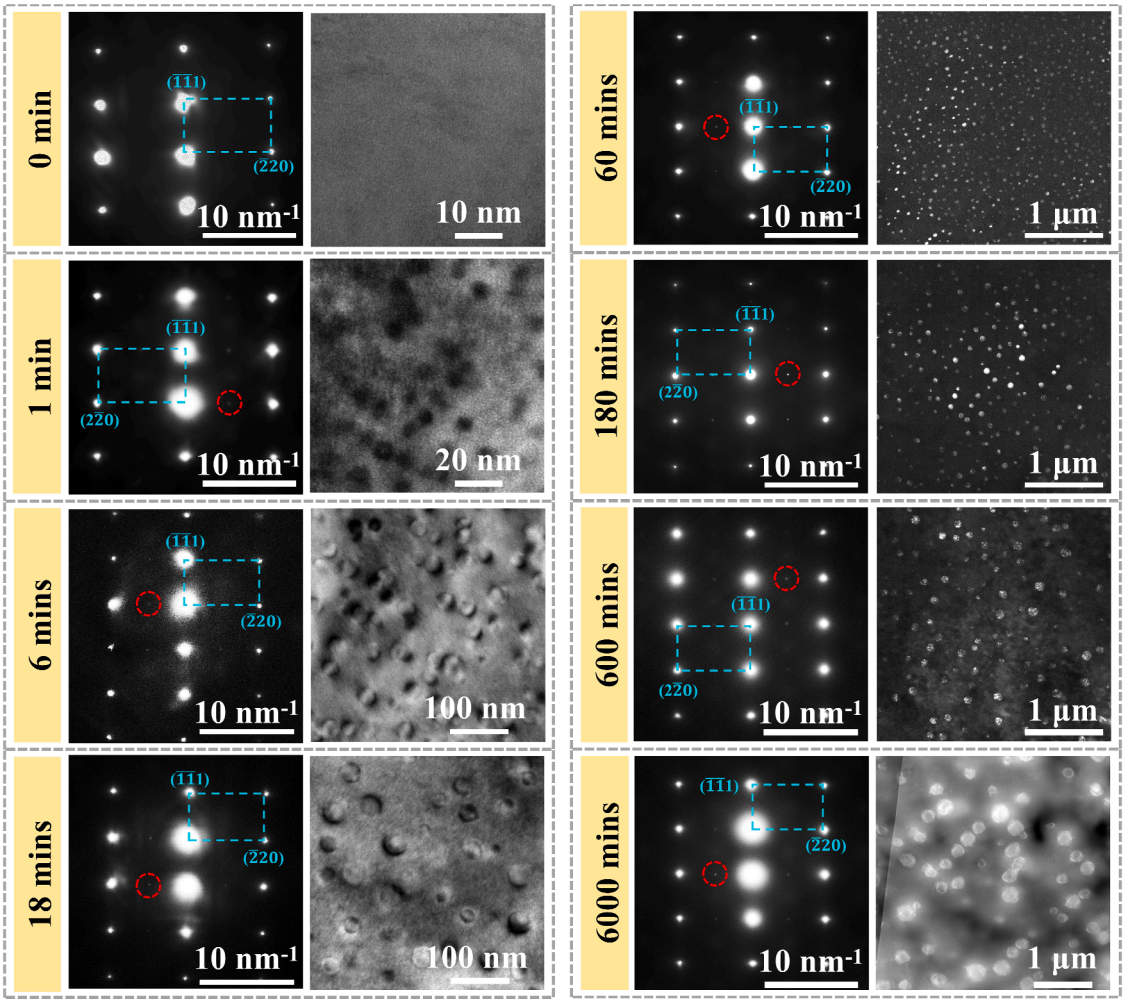

Fig. 2. SAED patterns with the [112] zone axis and TEM images of $(CoCrNi)_{94}Al_3Ti_3$ alloy in homogenized (0 min) and aged states. The TEM images for 60, 180, and 600 mins are dark-field images, whereas the rest are HAADF images.

Table 1
The area fraction (f), radius (r), number density (N_ρ), and inter-particle spacing (λ) of $L1_2$ phase in the $(CoCrNi)_{94}Al_3Ti_3$ alloy after aging for different times.

Aging time, t (mins)	Area fraction, f (%)	Radius, r (nm)	Number density, N_ρ (/μm^2)	Inter-particle spacing, λ (nm)
1	9.39 ± 0.23	2.89 ± 0.60	3578.66 ± 1064.60	10.94 ± 4.43
6	9.22 ± 0.23	10.18 ± 1.82	283.19 ± 74.30	39.06 ± 13.4
18	9.21 ± 0.33	13.85 ± 2.85	152.83 ± 43.95	53.19 ± 20.64
60	8.16 ± 0.35	18.14 ± 3.10	78.93 ± 18.89	76.28 ± 22.70
180	8.60 ± 0.90	25.66 ± 5.88	41.58 ± 11.18	103.77 ± 38.04
600	8.79 ± 0.70	40.20 ± 9.81	17.31 ± 5.24	159.93 ± 67.03
6000	11.00 ± 0.46	82.15 ± 20.34	5.19 ± 1.72	274.72 ± 137.27

3. Results

3.1. Microstructures

Fig. 1 shows the XRD plots of the $(CoCrNi)_{94}Al_3Ti_3$ MEA that was aged to different times, t. All the samples show a single phase with the FCC crystal structure. The lattice constant, a, estimated from the diffraction peaks is nearly constant at ~3.58 Å in all the samples. The slight change in the intensities of the diffraction peak may be due to the fact that the detection area only involves a few grains (the grain sizes of all samples are greater than 100 μm).

Representative TEM images along with the respective selected area electron diffraction (SAED) patterns (obtained along the [112] zone axis) for the alloys aged to different t are presented in Fig. 2. The SAED pattern of the homogenized sample corresponds to that of a single FCC phase. In all the aged samples, however, additional spots can be observed, indicating the presence of $L1_2$ superlattice structure in them [8]. In Fig. 2, the dark-field TEM images (or high-angle annular dark-field (HAADF) images), which were obtained using the superlattice spots, reveal the corresponding precipitated $L1_2$ particles with various sizes. The ImageJ software (National Institutes of Health) [33,34] was employed to estimate the area fraction, f, and radius, r, of the $L1_2$ phase from such images. The values of f and r, as well as the number density, N_ρ, and inter-particle spacing, λ, of the $L1_2$ phase are listed in Table 1. It shows that r increases from 2.89 nm at $t = 1$ min to 82.15 nm in the sample aged for 6000 mins, whereas the f value remains nearly unchanged at ~8–11 %, (see Figure S1 in supplementary information, SI). Meanwhile, N_ρ and λ sharply decreased and increased, respectively, with aging time. All these parametric changes with t indicate the coarsening process of $L1_2$ precipitates, as expected.

The coarsening process of $L1_2$ phase is driven by the interfacial free energy between the precipitate and the matrix, i.e., Ostwald ripening

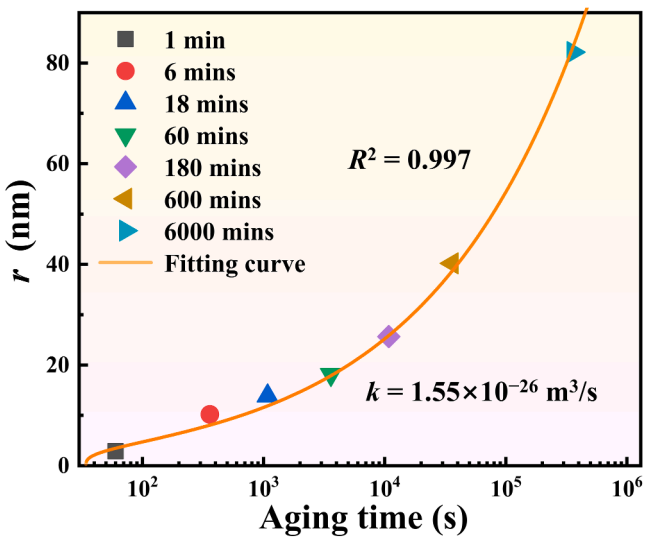

Fig. 3. LSW relationship illustrating the coarsening of the $L1_2$ phase in the aged $(CoCrNi)_{94}Al_3Ti_3$ alloy.

[35]. The coarsening kinetics of the nanoscale $L1_2$ particles in conventional FCC structured alloys have been extensively investigated, especially in Al alloys [36] and Ni-base superalloys [37–40]. As per the Lifshitz-Slyozov-Wagner (LSW) theory, the Ostwald ripening process can be described as [41–43]:

$$r^3(t) - r^3(t_0) = k(t - t_0) \tag{1}$$

where $r(t)$ is the average radius of the particles after being aged for a duration of t, and k is the coarsening rate constant. Fig. 3 shows the variation of r with t, and the fit of Eq. (1) into the data. The value k from the best fit is determined to be 1.55×10^{-26} m^3/s, which is ~2–4 orders of magnitude higher than those reported for $(CoCr_xNi)_{94}Al_3Ti_3$ ($x = 0.1$, 0.2 and 0.4) alloys that are aged at lower temperatures (750 °C) [43,44] compared to the higher aging temperature of the present study (950 °C).

High-resolution TEM (HRTEM) images of the precipitate-matrix interfaces for a few representative samples ($t = 6$, 60, and 600 mins), along with the Fast Fourier transformation (FFT) patterns of the matrix and $L1_2$ phases, are displayed in Fig. 4. It is seen that the precipitates and the matrix have coherent interfaces. The lattice mismatch, δ, between them can be expressed as [45,46]:

$$\delta = \frac{2(a^p - a^m)}{a^p + a^m} \tag{2}$$

where a^p and a^m are the lattice constants of the precipitate and the matrix, respectively. The values of a^p and a^m estimated from the HRTEM images are 3.582 and 3.569 Å, respectively. They result in a fairly small computed δ value of 0.36 %, which is similar to that reported for the $L1_2$ particles in $(CoCrNi)_{92}Al_6Ta_2$ alloy (δ =0.31 %) [43].

3.2. Critical strength for incipient plasticity

In Fig. 5, all the representative P-h curves exhibit distinct discrete displacement bursts or 'pop-ins', with a wide distribution in the load at the first pop-in, P_I. The Hertzian contact mechanics model [30] can be used to describe the elastic segment prior to the first pop-in, using the following the relation:

$$P = \frac{4}{3} E_r \sqrt{R_i h^3} \tag{3}$$

where R_i is the tip radius of the indenter, and E_r is the reduced modulus that can be determined using the $1/E_r = (1 - \nu_i^2)/E_i + (1 - \nu_s^2)/E_s$, where ν is the Poisson's ratio (=0.3, measured using the ultrasonic pulse-echo technique), E is the Young's modulus, and the subscripts i and s stand for the indenter and sample, respectively. By fitting Eqn. (3) into the P-h curves up to the first pop-in, the E_r values are obtained. Variations of E_r with t are plotted in Fig. 6. (In this figure and hereafter, the homogenized sample is represented with $t = 1$ s, since $t = 0$ cannot be plotted in a log scale). The E_r, E, and shear modulus G data are given in Table S1 of the SI. It is noted from Fig. 6 that E_r of the alloy does not vary in any significant manner with t and fluctuates marginally at ~248 GPa.

The shear strength corresponding to the onset of plasticity can be estimated as the maximum shear stress (that occurs at a depth of approximately 0.48 of the contact radius, a_c, underneath the indenter tip) at the first pop-in load [30]:

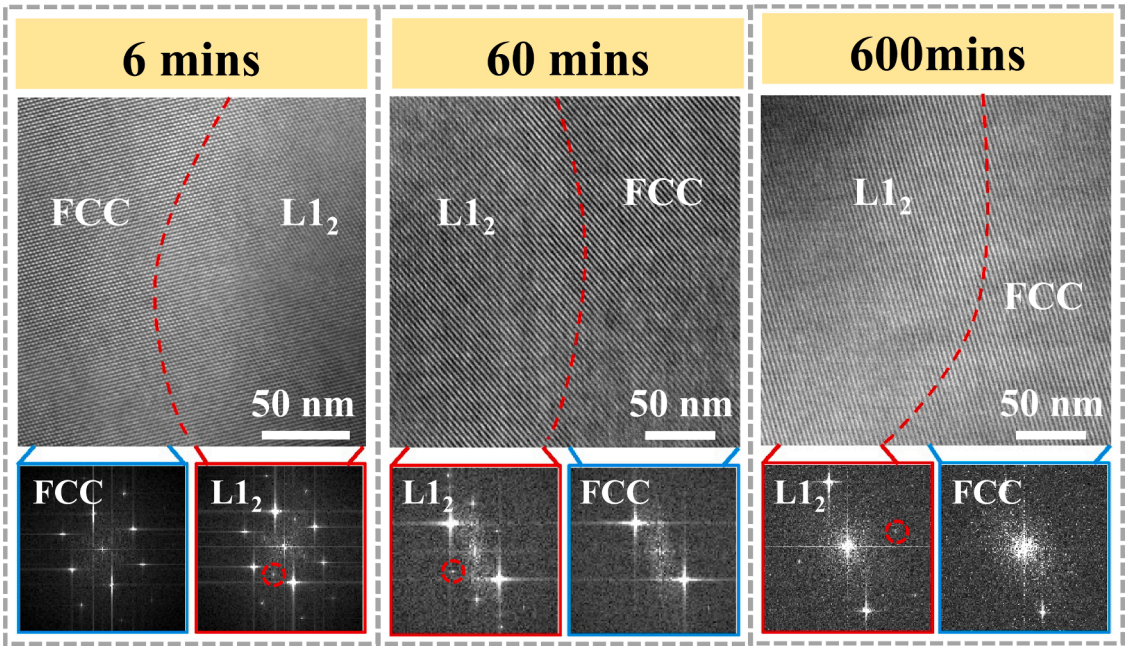

Fig. 4. HRTEM images of $(CoCrNi)_{94}Al_3Ti_3$ alloy after aging for 6, 60, and 600 mins show the $L1_2$-matrix interfaces, and FFT patterns of the two phases.

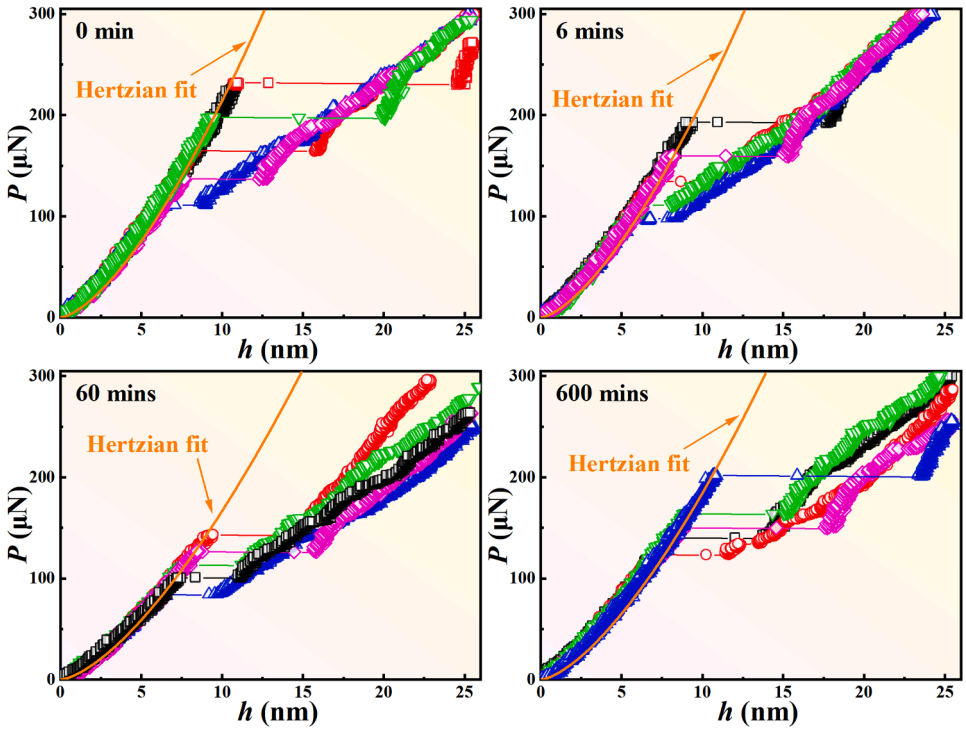

Fig. 5. Representative load-displacement (*P*-h) curves of $(CoCrNi)_{94}Al_3Ti_3$ alloy in homogenized state (0 min) and after aging for 6, 60, and 600 mins.

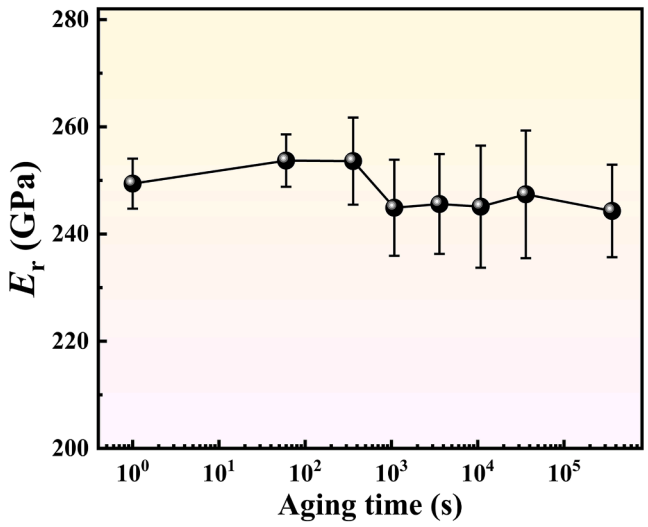

Fig. 6. The variation of the reduced modulus, E_r, of $(CoCrNi)_{94}Al_3Ti_3$ alloy with aging time *t*.

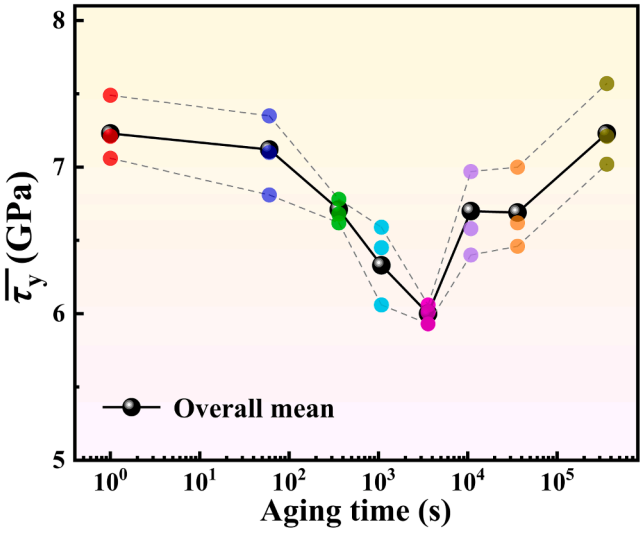

Fig. 7. The evolution of the $\overline{\tau_y}$ with *t* for each test grain (color dots) and the overall (dark dots). Three colored dots of the same color represent three random grains of the same sample for testing.

Table 2
Summary of minimum, maximum, mean ($\overline{\tau_y}$), standard deviation (SD), and coefficient of variation (CoV) values of τ_y for all the samples.

	τ_y (GPa)				
Aging time (mins)	Min.	Max.	$\overline{\tau_y}$	SD	CoV
0	4.79	8.18	7.23	0.71	10 %
1	5.34	8.26	7.12	0.64	9 %
6	5.16	8.25	6.71	0.68	10 %
18	4.44	8.80	6.34	0.85	13 %
60	4.33	7.77	6.00	0.67	11 %
180	4.63	8.15	6.70	0.70	10 %
600	4.70	8.28	6.69	0.68	10 %
6000	3.29	8.75	7.23	0.84	12 %

$$\tau_y = \frac{0.47}{\pi}\left(\frac{4E_r}{3R_i}\right)^{2/3} P_1^{1/3} \tag{4}$$

Values of τ_y, including minimum, maximum, mean ($\overline{\tau_y}$), standard deviation (SD), and coefficient of variation (CoV) (defined as the ratio of standard deviation to the mean value) are summarized in Table 2. In all cases, the variation in the CoV values (ranging from 9 % to 13 %) is not significant. With an increasing *t*, $\overline{\tau_y}$ first reduces, reaching a minimum at $t = 60$ mins, before increasing again. This trend is consistent across all the grain orientations studied, as demonstrated by the same trend observed in each orientation as shown in Fig. 7.

The statistical nature of τ_y is illustrated in Fig. 8, represented as

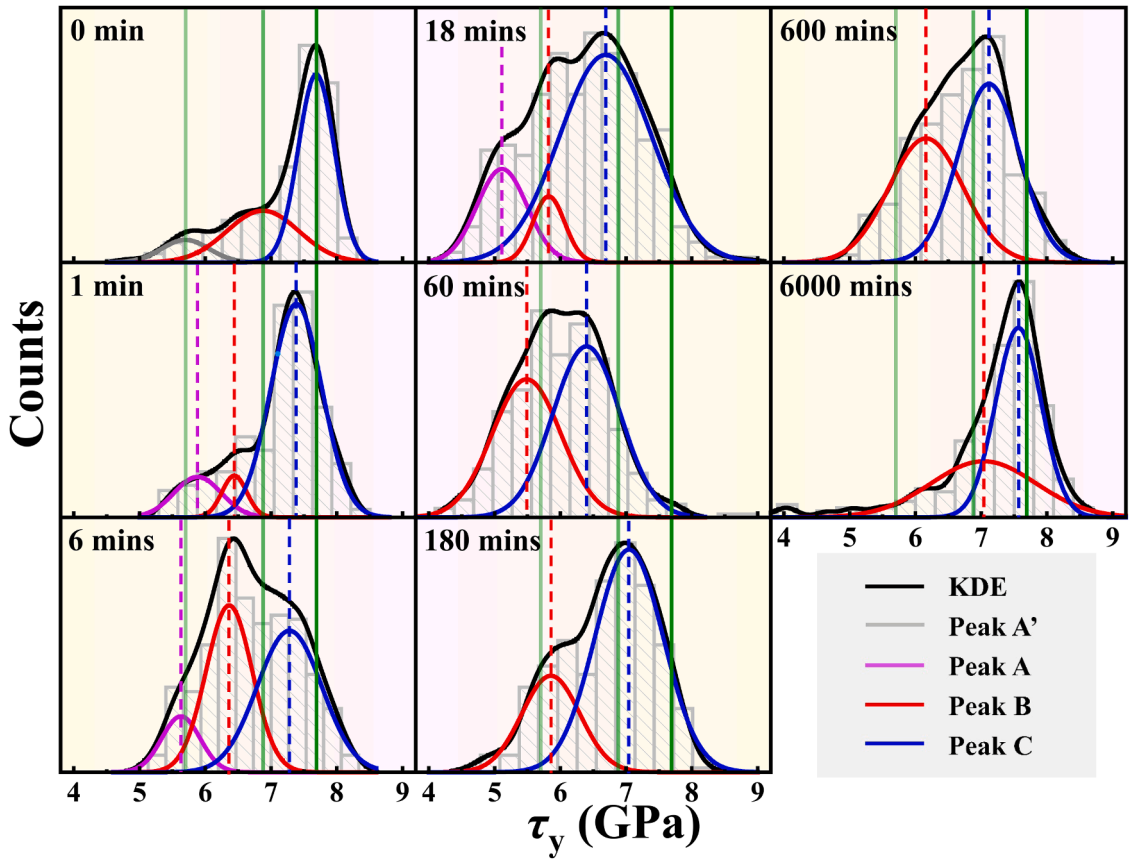

Fig. 8. Histograms, KDE plots, and deconvolution results by Gaussian distributions for the τ_y of homogenized (0 min) and aged samples. The deconvolution peaks with different colors represent different deformation mechanisms, which are named peaks A (or A'), B, and C, respectively. The vertical green lines mark the peak locations in the homogenized sample as a benchmarking reference for the curves of the aged samples.

Table 3
The results of peak fitting based on Gaussian distribution.

Aging time (mins)	Peak	$\overline{\tau_y}$(GPa)	AF	Peak	$\overline{\tau_y}$(GPa)	AF	Peak	$\overline{\tau_y}$(GPa)	AF
0	A'	5.70	0.09	B	6.88	0.32	C	7.69	0.59
1	A	5.88	0.14	B	6.44	0.07	C	7.38	0.79
6	A	5.63	0.11	B	6.36	0.41	C	7.28	0.48
18	A	5.11	0.18	B	5.82	0.08	C	6.69	0.74
60				B	5.49	0.48	C	6.40	0.52
180				B	5.86	0.27	C	7.04	0.73
600				B	6.16	0.46	C	7.12	0.54
6000				B	7.04	0.41	C	7.57	0.59

histograms and the kernel density estimate (KDE) plots [16,47,48]. In most cases, τ_y is bimodal in nature. In a few cases, it appears to be tri-modal. To ascertain this, the obtained KDE plots are deconvoluted, assuming that each constituent distribution is also Gaussian in nature, represented as [16,18,19]:

$$f(\tau_y) = \frac{1}{S\sqrt{2\pi}} \exp\left(-\frac{\left(\tau_y - \overline{\tau_y}\right)^2}{2S^2} \right) \tag{5}$$

The deconvolution results are also plotted Fig. 8, using different colors with each color representing a different deformation mechanism that will be discussed later. The dashed straight lines of the same color represent the corresponding $\overline{\tau_y}$ of each fitted peak. In the homogenized state, a trimodal distribution of τ_y is noted. This persists up to $t = 18$ mins. For longer times of aging, i.e., for $t \geq 60$ mins (and up to 6000 mins), the distribution of τ_y is bimodal. The $\overline{\tau_y}$ of the three fitted peaks in the homogenized sample are marked with green straight lines. For clarity, these peaks are labelled as A (or A'), B, and C from lower to higher stress levels. Note that only peaks B and C are present in the samples aged for 60–6000 mins. The $\overline{\tau_y}$ and area fractions (AFs) of all the peaks for the samples to different t are listed in Table 3. As t increases, $\overline{\tau_y}$ of peaks B and C increase after the initial decline, whereas that of peak A decreases until the peak disappears after aging for 60 mins or longer.

4. Discussion

4.1. Different defects and their distributions

The reported values of the critical resolved shear stress, τ_c, for dislocation glide in FCC HEAs (for example, they are ~33–60 MPa for CoCrFeMnNi [49,50]) are substantially smaller than the experimentally recorded minima irrespective of the aging condition for the $(CoCrNi)_{94}Al_3Ti_3$ alloy examined in this study. This observation leads us to conclude that the dislocation nucleation is the only possible mechanism responsible for the first pop-ins of the current study. The presence or absence of defects at the location (and the finite volume surrounding it)

Table 4
Summary of the vacancy formation energy u_n reported in the literature and the estimated results of the concentration and average spacing of monovacancy and divacancy at 1200 and 950 °C.

u_n (eV)	T (°C)	ρ_{Monov}	l_{Monov} (nm)	ρ_{Div}	l_{Div} (nm)
1.73 [54]	1200	2.97×10^{-6}	16	2.57×10^{-10}	355
	950	1.83×10^{-7}	40	1.35×10^{-12}	2040

of the maximum shear stress underneath the indenter determines whether the dislocation nucleation occurs heterogeneously or homogenously. To decipher these two mechanisms, it is essential to assess the densities of different defects and the spacings between them in the alloy.

In the prior research performed on the incipient plasticity of crystalline alloys, the defects that may cause the heterogeneous nucleation of dislocations have been identified as monovacancies, vacancy clusters, and dislocations [51]. Note that a coherent interface, as an important 2-dimensional crystalline defect, will play the same role as the other defects, and its distribution parameters have been calculated above. The mean spacing between the pre-existing dislocations in well annealed metals would be ~1 μm (assuming a dislocation density is $\sim 10^{12}$ m^{-2} [16,52]).

The thermodynamics of intrinsic point defects (vacancies) in pure metals follows the Arrhenius law: $\rho_1 = \exp[-u/kT]$, where ρ_1 is the equilibrium concentration of the monovacancies, u is their formation energy, k is the Boltzmann constant, and T is the absolute temperature. Wang *et al.* derived the monovacancy equilibrium concentration in an equiatomic HEA as [53]:

$$\rho_n = \frac{\exp\left(n-1-\frac{u_n}{kT}\right)}{n+\exp\left(n-1-\frac{u_n}{kT}\right)} \tag{6}$$

where n represents the number of principal elements in HEA and u_n is the formation energy of a vacancy in it. Assuming that the u does not change with the number of the components in the alloy, ρ_n/ρ_1 can be expressed as [53]:

$$\frac{\rho_n}{\rho_1} = \frac{\exp(n-1)}{n+\exp\left(n-1-\frac{u_n}{kT}\right)} \approx \frac{\exp(n-1)}{n} \tag{7}$$

Because of the low contents of Al and Ti, the $(CoCrNi)_{94}Al_3Ti_3$ alloy examined here can be considered as ternary HEA, i.e., $n = 3$.

The reported values of u_n in the CoCrFeMnNi HEAs range between ~1.69 and 2.00 eV [54–57]. Chen *et al.* [54] estimated u_n of each element in the FeCoCrNi alloy using the first principles calculations, and then used the rule of mixtures to arrive at an u_n of 1.73 eV for CoCrNi HEA. Using this value for the current $(CoCrNi)_{94}Al_3Ti_3$ in Eqn. (7), the concentration ρ_{Monov} and average spacing, $l_{Monov} = [(1/\rho_{Monov})/\text{number of atoms percell}]^{1/3} \times a$, of the monovacancy are obtained and listed in Table 4. It is seen that l_{Monov} of the alloy at the homogenizing and aging temperatures (1200 and 950 °C, respectively) are 16 and 40 nm, respectively. (Although the nanoindentation experiments are performed at room temperature (RT) and hence the inferences regarding the mechanical behavior all pertain that at RT, the vacancy concentrations correspond to those at high temperatures as it is implicitly assumed that they remain as the cooling rates to RT subsequent to homogenization or aging are relatively high.)

When two adjacent monovacancies form a divacancy, the number of missing bonds in the alloy will be reduced from $2z$ (for two independent monovacancies) to $2z-1$, where z is the coordination number. It is conceivable that the formation of divacancies will lower the internal energy of the alloy. Based on the binding energy between vacancies, U, the concentration of divacancies, ρ_{Div}, can be written as [58]

$$\rho_{Div} = \frac{z}{2}\rho_{Monov}^2 \exp\left(\frac{U}{kT}\right) \tag{8}$$

Table 5
Summary of $\overline{\tau_y}$ values, contact radius a_c and corresponding dislocation nucleation mechanism of all fitting peaks for all the samples. Where 'Homo' denotes homogeneous nucleation, 'Hetero' denotes heterogeneous nucleation, 'interfaces' and 'matrix' indicate the location of the nucleation sites.

Aging time (mins)	Peak	$\overline{\tau_y}$(GPa)	a_c (nm)	Mechanisms
0	A'	5.70	50	Hetero-divacancies
	B	6.88	60	Hetero-monovacancies
	C	7.69	67	Homo
1	A	5.88	50	Hetero-monovacancies (interfaces)
	B	6.44	55	Hetero-monovacancies (matrix)
	C	7.38	63	Hetero (interfaces)
6	A	5.63	48	Hetero-monovacancies (interfaces)
	B	6.36	54	Hetero-monovacancies (matrix)
	C	7.28	62	Hetero (interfaces)
18	A	5.11	45	Hetero-monovacancies (interfaces)
	B	5.82	52	Hetero-monovacancies (matrix)
	C	6.69	59	Hetero (interfaces)
60	B	5.49	49	Hetero-monovacancies
	C	6.40	57	Homo or Hetero (interfaces)
180	B	5.86	52	Hetero-monovacancies
	C	7.04	63	Homo or Hetero (interfaces)
600	B	6.16	54	Hetero-monovacancies
	C	7.12	63	Homo or Hetero (interfaces)
6000	B	7.04	63	Hetero-monovacancies
	C	7.57	68	Homo or Hetero (interfaces)

The value of U is typically taken as 0.2 eV [58]. The estimated values of ρ_{Div} and average spacing l_{Div} of the divacancies are as following: at 1200 °C, $\rho_{Div} = 2.57 \times 10^{-10}$, $l_{Div} = 355$ nm; at 950 °C, $\rho_{Div} = 1.35 \times 10^{-12}$, $l_{Div} = 2040$ nm.

4.2. Dislocation nucleation mechanisms

The radius of the contact area between the indenter and the sample surface during nanoindentation, *i.e.*, the contact radius, a_c, can be expressed as [15]:

$$a_c = \left(\frac{3P_I R_i}{4E_r}\right)^{1/3}. \tag{9}$$

Using a_c, the volume of the highly stressed zone underneath the indenter, V_s, can be estimated as $V_s = \pi a_c^3$ [13,21]. The values of a_c corresponding to peaks A, B, and C for samples aged to different t are given in Table 5. The values range from 45 to 68 nm. On comparing with the estimated average spacing of mono- and di-vacancies in the homogenized sample (16 and 355 nm, respectively), it is reasonable to expect that the sources for heterogeneous dislocation nucleation can be either monovacancies or divacancies (with the latter occurring at a much reduced probability). In all the aged samples, however, dislocation nucleation from monovacancies or coherent interfaces is possible, since the inter-spacings of both divacancies (~2 μm) and dislocations (~1 μm) are significantly larger than a_c. In addition, some prior works reported in literature suggest that the first pop-in can also be triggered by homogeneous dislocation nucleation, but at a substantially higher stress that approaches the theoretical strength of a perfect crystal [11,16,18,19,59]. For visualizing the dislocation nucleation mechanism responsible for each of the τ_y peaks observed in Fig. 8 and the effect of $L1_2$ phase with various sizes, the spacings of monovacancies, divacancies, and $L1_2$ phases in $(CoCrNi)_{94}Al_3Ti_3$ alloy, as well as the contact radius a_c, the stressed volume (with respect to the location of the indenter tip) are schematically illustrated (but drawn to scale) in Fig. 9.

For the homogenized sample, $\overline{\tau_y}$ of peak C is determined to be about G/14, which is in the range of the theoretical shear strength (G/30–G/5) [25,60]. This observation leads us to infer that this peak is caused by homogeneous dislocation nucleation, when the indentation is made on a

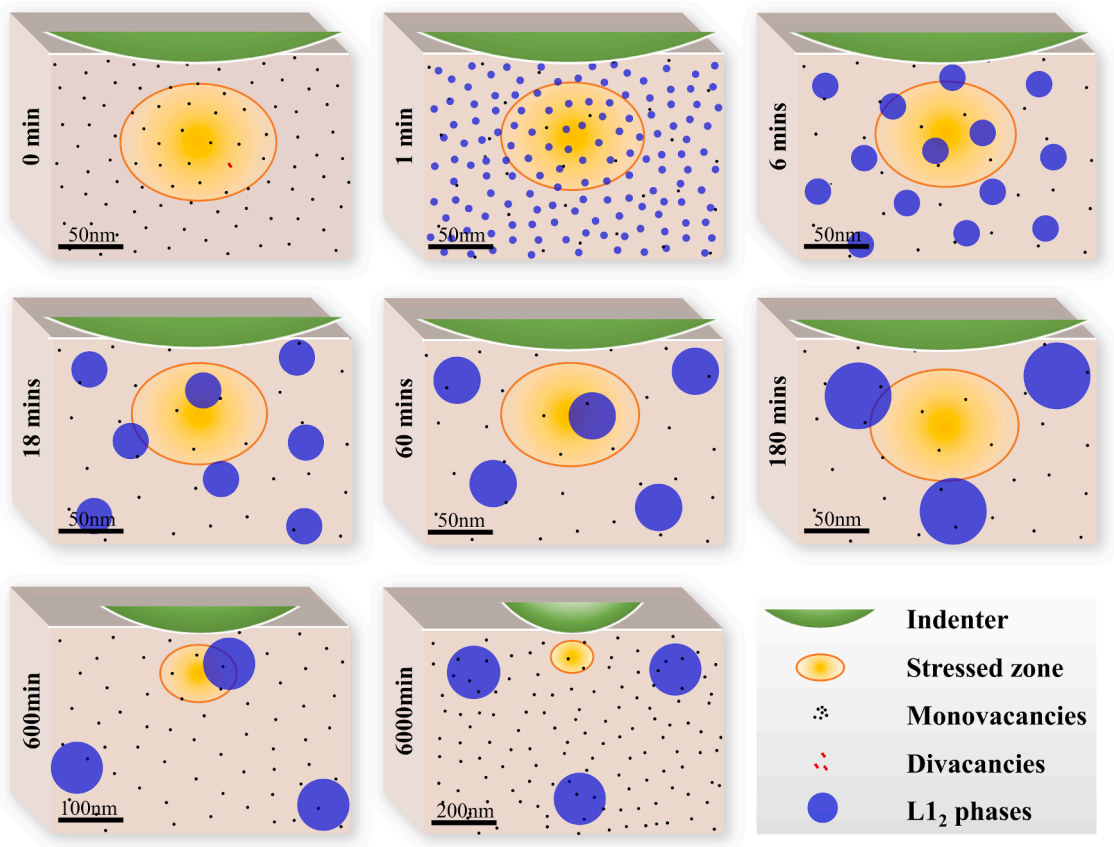

Fig. 9. Distribution diagram of monovacancies, divacancies and $L1_2$ phases in $(CoCrNi)_{94}Al_3Ti_3$ alloy under indenter after homogenization and aging for different t, where the average spacing of defects, the r and L of $L1_2$ phase, the contact radius a_c, the volume of stressed zone V_s, and the penetration depth of the indenter are reduced proportionally. (Note that the scales of 600 and 6000 mins are different from others.).

defect-free domain of the grain [15,16]. When it comes to peaks A' and B, heterogeneous dislocation nucleation with different sources is likely to have taken place. As shown in Fig. 9, the range of a_c is between ~50–67 nm. When the sample is indented, the probability of the stressed volume containing a divacancy is ~0.14, while several monovacancies are most likely to be present within the stressed volume. Furthermore, the lattice distortion induced by divacancies is more severe (compared to that caused by a monovacancy). This may lower the τ_c required for triggering the first pop-in more significantly than that by monovacancy [61]. On this basis, we hypothesize that the peak A' with the lowest τ_y, which also has the lowest area fraction in the τ_y distribution, is likely caused by the divacancy-induced heterogeneous nucleation mechanism. Consequently, peak B is possibly due to the monovacancy-induced heterogeneous nucleation mechanism.

Upon aging, the average spacing between the divacancies increases substantially to 2040 nm, lowering the probability of a divacancy being present in the highly stressed volume to ~0.02. Additionally, the presence of divacancies in the stressed volume does not necessarily lead to heterogeneous nucleation, due to the inhomogeneous distribution of the applied stress underneath the indenter. Therefore, divacancy-induced dislocation nucleation is highly unlikely in the aged samples. On the other hand, the mean spacing between monovacancies, which also increases but only to 40 nm, remains smaller than a_c. Thus, the monovacancies remain as the major sources for heterogeneous dislocation nucleation in all the aged samples.

When the size of $L1_2$ phase is small (for t = 1 to 18 mins), the combination of high N_ρ and low λ determines that the stressed material volume should contain several monovacancies and $L1_2$ phases, as shown in Fig. 9. For the peak C of these samples, $\overline{\tau_y}$ is around G/16–G/15, suggesting heterogeneous dislocation nucleation induced by coherent interface. Driven by the lattice mismatch of the interfaces between the $L1_2$ phase and the matrix, the stress required for the dislocation nucleation near the coherent interface is likely to be reduced [9,62]. The coherent interfaces preserve the continuity of the lattice structure, and the tiny lattice distortion determines the slight decrease of the $\overline{\tau_y}$ for peak C compared to the homogenized sample (~G/14). Since the monovacancies also have a high probability of appearing near the coherent interfaces [63], which is aided by the lattice mismatch, dislocation nucleation at the monovacancies near the interfaces is easier than that in the matrix (far away from the interfaces). Therefore, peak A, with the lowest $\overline{\tau_y}$, probably stems from a monovacancy-induced heterogeneous dislocation nucleation near the precipitate/matrix interface. Then, peak B is probably mediated by the monovacancy-induced heterogeneous dislocation nucleation far from the interface.

As the $L1_2$ phase continues to coarsen (t = 60 to 6000 mins), as shown in Fig. 9, the number density of the coherent interface in the stressed zone underneath the indenter decreases sharply. This, in turn, markedly reduces the likelihood of finding monovacancies that are located near the precipitate/matrix interfaces within the stressed volume. This results in the disappearance of peak A for these samples. Moreover, compared with the aged samples for t up to 18 mins discussed above, the distribution of the monovacancies shows no significant difference, but the population of the interfaces in the stressed zone decreases. Based on this, we hypothesize that the peak B is likely to be governed by monovacancy-induced heterogeneous nucleation, and peak C is dominated by homogeneous nucleation in the matrix or heterogeneous nucleation with the assistance of the coherent interfaces, depending on the location of the indentation (with respect to the nearest interface) and the spacing between the precipitates. For all the samples, identical deformation mechanisms are marked with the same color

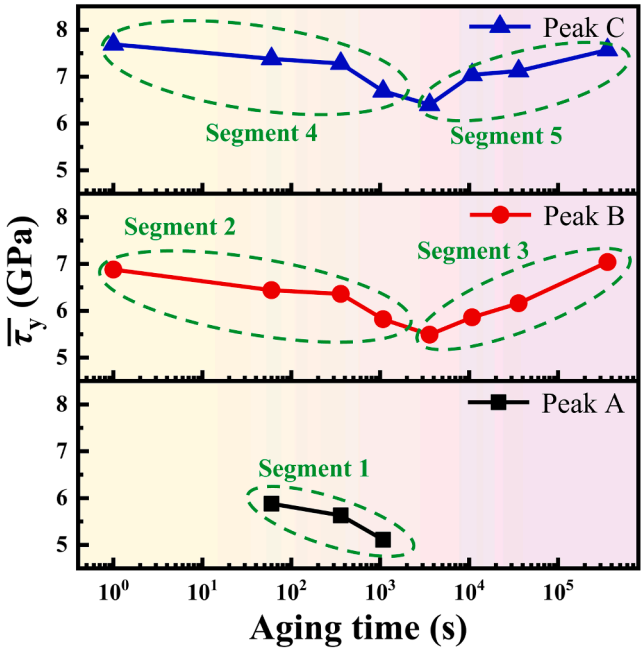

Fig. 10. The evolution of $\overline{\tau_y}$ with t for Peak A, B, and C. And it is divided into five segments according to their mechanism and the evolution trend of $\overline{\tau_y}$.

(homogeneous nucleation and coherent interface-induced heterogeneous nucleation are marked with the same color), as shown in Fig. 8. The values of $\overline{\tau_y}$, a_c, and the inferred deformation mechanism for each deconvolution peak are also presented in Table 5.

4.3. *The effect of $L1_2$ phase coarsening on the critical strength for incipient plasticity*

The aforementioned results demonstrate that, in the $L1_2$-precipitated $(CoCrNi)_{94}Al_3Ti_3$ alloy, dislocation nucleation preferentially occurs at or near the coherent interfaces of the precipitates and the matrix, due to the lower activation stress required, which is consistent with the atomistic simulation results reported in the literature [9]. It appears, however, that the size of the $L1_2$ phase exerts a distinct effect on the dislocation nucleation mechanism, as reflected by the different $\overline{\tau_y}$ values of the same peak in different aged samples. In the initial stages of aging, i.e., when t is between 1 and 18 mins, $\overline{\tau_y}$ decreases with t, where for larger t (60 to 6000 mins) $\overline{\tau_y}$ increases. This results in $\overline{\tau_y}$ being the lowest in the samples aged for 60 mins, suggesting that the dislocation nucleation in it is the easiest and hence, possibly the most promising for exhibiting large plasticity [9]. In the following discussion, the evolutionary characteristics of $\overline{\tau_y}$ with aging for peaks A, B, and C are divided into five segments, as marked in Fig. 10. Since only the peak A' of the homogenized sample is induced by the divacancies, it is not included in Segment 1.

As mentioned above, the coherent interfaces can serve as dislocation sources, governed by the lattice mismatch (δ = 0.36 %) between the precipitates and the matrix. The lattice mismatch amplifies the distortional strains at the interface, which can aid in the reduction of the activation energy barrier for dislocation nucleation [9]. Results of the current study indicate that the misfit strain required to activate the dislocation nucleation may be related to the size of the precipitates. The larger the size of the $L1_2$ phase, the lower will be the barrier for the dislocation nucleation [9]. Note that this is only true for cases where there are sufficient number of the coherent interfaces in the highly stressed volume underneath the indenter. In the samples aged up to 18 mins, the density of the coherent interfaces in the stressed zone is large (see Fig. 9). Therefore, both the $\overline{\tau_y}$ of Segment 1, which is dominated by the monovacancy-induced heterogeneous nucleation near the coherent interface, and that of the Segment 4, which is governed by the coherent interface-assisted heterogeneous dislocation nucleation, exhibit a downward trend with the growth of $L1_2$ phase.

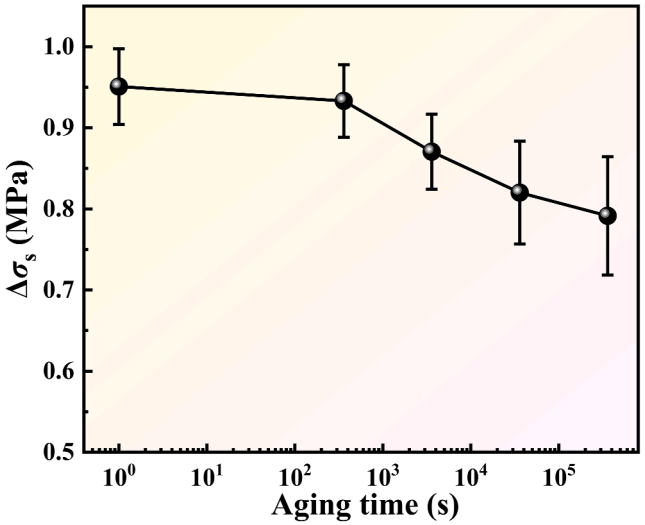

Fig. 11. Evolution of solid solution strengthening of matrix phase with t.

Since Segment 2 is governed by the monovacancy-induced heterogeneous dislocation nucleation within the matrix, the precipitate/matrix interfaces would have no role to play in determining $\overline{\tau_y}$. The precipitation process during aging is accompanied by the diffusion of certain elements to the $L1_2$ phase [37,41]. For example, the $L1_2$ phase in the $(CoCrNi)_{94}Al_3Ti_3$ alloy was shown to be (Ni, Co, Cr)$_3$(Ti, Al)-type and is rich in Ni, Al, and Ti elements [8]. Table S2 in the SI gives the measured chemical compositions of $L1_2$ phase by TEM equipped with an energy dispersive X-ray spectrometer (EDS) after aging for 6, 60, 600, and 6000 mins. It shows that the precipitates get enriched in Ni and Ti, while getting depleted in Co and Cr, as they coarsen (the variations in the Al content are within the scatter). The compositional alterations of the $L1_2$ phase may exert a pronounced influence on the yield stress and the reduced modulus of the alloy, which can be delved into by molecular dynamics simulations [64]. Nevertheless, the absence of an applicable interatomic potential for the $(CoCrNi)_{94}Al_3Ti_3$ alloy renders it arduous to conduct in-depth interpretations at present.

Here, if Co, Cr, and Ni are regarded as solvent atoms and Al and Ti are solute atoms, the strength enhancement due to the solid solution strengthening, $\Delta\sigma_s$, can be estimated using the relation [7,65,66]:

$$\Delta\sigma_s = M\cdot\frac{G\cdot\varepsilon_s^{3/2}\cdot c^{1/2}}{700} \tag{10}$$

where c is the total molar ratio of Al and Ti in the matrix, $M = 3.06$ is the Taylor factor, and the interaction parameter ε_s is:

$$\varepsilon_s = \left|\frac{\varepsilon_G}{1+0.5\varepsilon_G} - 3\varepsilon_a\right| \tag{11}$$

which combines the effects of elastic and atomic size mismatches, i.e., ε_G and ε_a, which are defined as:

$$\varepsilon_G = \frac{1}{G}\frac{\partial G}{\partial c} \tag{12}$$

$$\varepsilon_a = \frac{1}{a}\frac{\partial a}{\partial c} \tag{13}$$

ε_G is typically negligible compared to ε_a. The predicted trends in $\Delta\sigma_s$, made using the estimated values of ε_a, with t are presented in Fig. 11. The solute atoms in the matrix gradually decrease as the aging proceeds, which tends to lower the $\Delta\sigma_s$ of the matrix and cause the $\overline{\tau_y}$ of Segment 2

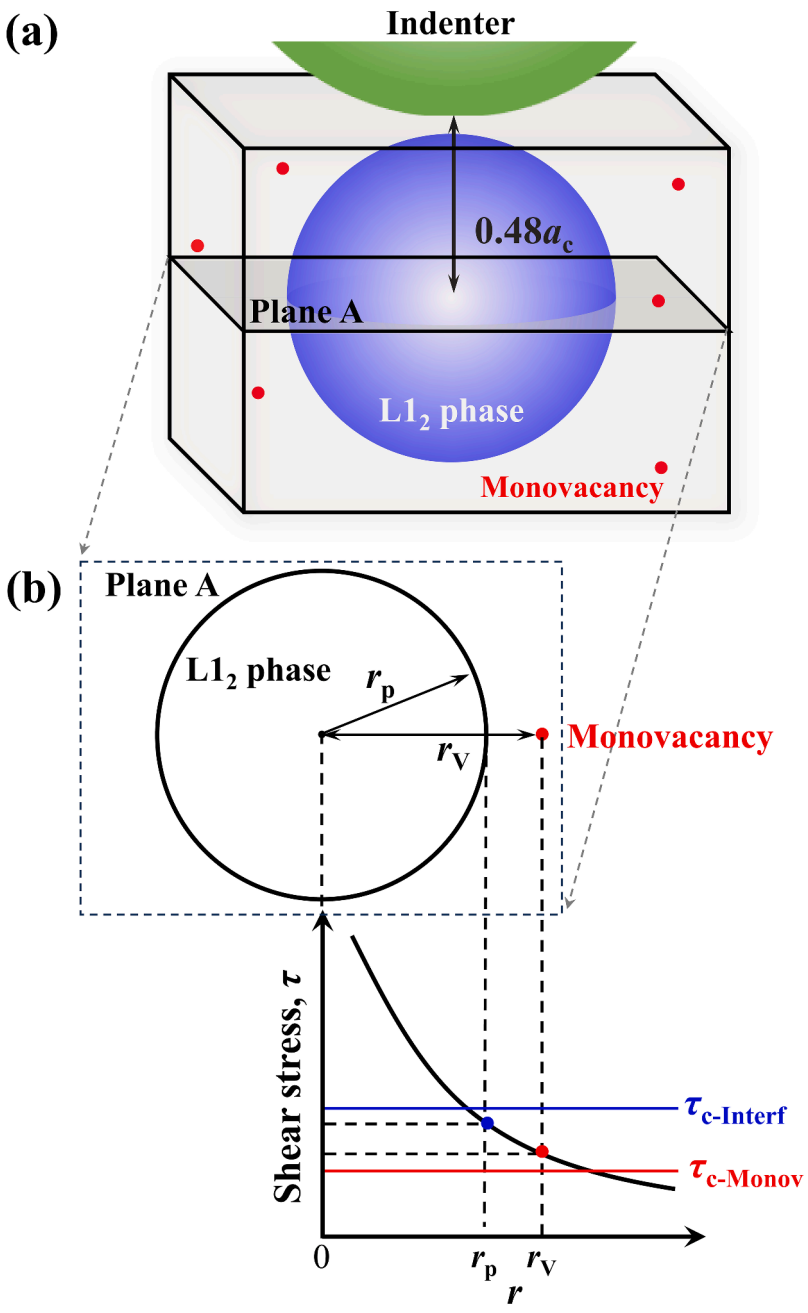

Fig. 12. (a) When the maximum shear stress at 0.48 a_c directly under the indenter is at the center of a large $L1_2$ phase, (b) a schematic illustration of the change of shear stress along the polar diameter r in a polar coordinate system with the center of $L1_2$ phase as the pole on Plane A. $\tau_{c\text{-Interf}}$ represents the shear stress required for coherent interface-assisted heterogeneous dislocation nucleation, and $\tau_{c-Monov}$ represents the shear stress required for monovacancy-induced heterogeneous dislocation nucleation.

to show a downward trend. Although the deformation mechanism of Segment 3 is the same as that of Segment 2 and is also affected by solid solution strengthening, these two segments show opposite trends with aging, implying that Segment 3 is more significantly affected by other factor(s).

After aging from 60 to 6000 mins, the radius of $L1_2$ phase increases from 18.14 to 82.15 nm. Since a_c is in the range of ~49–68 nm, it is possible that the indenter may act directly above a large $L1_2$ phase 'island' in these aged samples and the maximum shear stress, τ_{max}, is exerted on its center, as illustrated in Fig. 12(a). In this case, the ultra-high strength of the $L1_2$ phase makes it impossible for dislocations to nucleate internally [67]. Consequently, and for the occurrence of the first pop-in, the dislocations must nucleate near the interface or at the monovacancies in the matrix. To simplify, we analyze the stress distribution on Plane A in Fig. 12 where the center of the $L1_2$ phase is located. In Fig. 12(b), a polar coordinate system is established with the phase center as the pole. From the center to the edge, the shear stress, τ, decay is inversely proportional to the radial distance [68–70]. When a monovacancy in the matrix is adjacent to the interface, as the external stress increases, τ at the monovacancy reaches the critical resolved shear stress for monovacancy-induced heterogeneous dislocation nucleation, $\tau_{c-Monov}$, preferentially and thus the first pop-in takes place. When no defect is present, a much higher external stress ($\tau_{c\text{-Interf}}$) that approaches the theoretical strength is required to initiate the heterogeneous dislocation nucleation near the interface. For the same applied τ_{max}, both $\tau_{c-Monov}$ and $\tau_{c\text{-Interf}}$ decrease with increasing $L1_2$ particle size. As a

result, the critical load, P_I, for the incipient plasticity increases with the coarsening of the $L1_2$ phase. This is also the reason why $\overline{\tau_y}$ of both Segments 3 and 5 show upward trends. In addition, due to the huge spacing between $L1_2$ phases, the probability for the indentation being made only on the matrix is high, leading to the homogeneous dislocation nucleation inside the matrix. This possibility also contributes to the increase in $\overline{\tau_y}$ in Segment 5 with t.

4.4. Correlation between the microscopic and macroscopic plastic properties

Before closing, it is instructive to examine if the microscopic strength properties (specifically $\overline{\tau_y}$) and the inferences made using their stochastic nature on the deformation mechanisms can be correlated to the macroscopic plastic properties. For this purpose, we conducted the Vickers hardness measurements as well as indentation plastometry analysis for estimating the tensile yield strength (YS) of the alloy samples that were aged to different extents. (Since the volumes of alloy samples are insufficient for conducting uniaxial tests, we estimated these properties by recourse to the indentation plastometry [25]. While cognizant of the fact that these properties thus estimated might not be accurate, we would like to highlight that the purpose is to only compare the trends with t and, in the process, attempt to connect the micro-scale incipient plasticity with the macro-scale properties.)

Precipitation of coherent second phases is an important strengthening mechanism for a wide range of alloys, including HEAs. Typically, the strength of the alloy that was in the supersaturated solid solution first increases with t, reaches a peak, and then decreases. The variation in the Vickers hardness with t, displayed in Fig. S2 of the SI, is consistent with such an expected general trend. The variation in YS, displayed in Fig. S3 of SI, with t is similar to that of Vickers hardness, as expected. The contrasting trends in the microscopic ($\overline{\tau_y}$) and macroscopic (hardness and YS) strength properties with t can be rationalized as following. First, it is important to recognize that the macroscopic properties reflect the mean field behavior of the alloy and encompass several different microstructural characteristics such as the grain size. Importantly, they involve the collective motion and multiplication of many dislocations. The incipient plasticity characteristics measured using nanoindentation, in contrast, are mainly concerned with the nucleation or the activation of existing dislocations, but only a few of them. In the context of the aged alloy, the macroscopic plastic behavior additionally depends on the size, shape, and distribution of the precipitate phase inside the alloy, while the microscopic strength depends on whether a single precipitate phase exists within the stressed zone and the nature of its interface with the matrix. The formation of the $L1_2$ phase during aging could exert different effects on the macroscopic yield strength and the pop-in stress, viz. enhancing the former and weakening the latter, as different mechanisms dominate the two processes. Similar scenarios have been reported for the distinct changes in the macroscopic versus microscopic yielding strengths in the effects of pre-straining [15,71] and grain refinement [27].

5. Summary

The nanoindentation studies conducted in this work examined the stochastic nature of the incipient plasticity in $(CoCrNi)_{94}Al_3Ti_3$ MEA that is precipitation hardened with the $L1_2$ phase of various sizes. As the average radius of $L1_2$ precipitate increases (from 3 to 82 nm) with aging, due to the Ostwald ripening, the critical strength for incipient plasticity, τ_y, first decreases and then increases, with the minimum occurring at $t =$ 60 mins. The distributions of τ_y are multimodal in nature, or more specifically, trimodal for the samples in homogenized state and aged up to 18 mins, whereas bimodal for the samples aged for 60 mins and more. By considering relative sizes of the indentation contact radius and the inter-spacing between various defects (dislocations, and mono- and di-vacancies) and $L1_2$ precipitates, the underlying deformation mechanisms for each of the deconvolution peaks in all the samples (homogenized as well as aged) were ascertained. In the aged samples, the mechanisms include monovacancy-induced heterogeneous dislocation nucleation in the matrix near and far from the precipitate/matrix interface that is coherent, as well as interface-assisted heterogeneous dislocation nucleation. It is suggested that the coherent interface plays a key role by lowering the critical stress required for the dislocation nucleation and hence can act as a unique dislocation nucleation source. By optimizing the coherency strain at such interfaces, it might be possible to design alloys with simultaneously improved strength and ductility.

CRediT authorship contribution statement

Qian Zhang: Writing – original draft, Investigation, Formal analysis, Data curation. **Junwei Qiao:** Supervision, Funding acquisition, Conceptualization. **Yakai Zhao:** Writing – review & editing, Investigation, Formal analysis. **Jae-il Jang:** Writing – review & editing. **Upadrasta Ramamurty:** Writing – review & editing, Supervision, Funding acquisition.

Declaration of competing interest

The authors declare that they have no known competing financial interests or personal relationships that could have appeared to influence the work reported in this paper.

Acknowledgements

The work at Taiyuan University of Technology was supported by the financial support of the National Natural Science Foundation of China (No. 52271110 and 52201188), Key Research and Development Program of Shanxi Province (No. 202102050201008), and Natural Science Foundation of Shanxi Province (No. 202203021221083). The work at Nanyang Technological University and IMRE was supported by Agency for Science, Technology and Research (A*STAR) of Singapore via the Structural Metal Alloys Programme (No. A18B1b0061). The work at Hanyang University was supported by the National Research Foundation of Korea (NRF) grants funded by the Korea government (MSIT) (no. 2022R1A5A1030054 and RS-2023–00273384). Q.Z. acknowledges the support from China Scholarship Council (CSC).

Supplementary materials

Supplementary material associated with this article can be found, in the online version, at doi:10.1016/j.actamat.2025.120826.

References

[1] T. Yang, Y.L. Zhao, Y. Tong, et al., Multicomponent intermetallic nanoparticles and superb mechanical behaviors of complex alloys, Science (1979) 362 (6417) (2018) 933–937.
[2] Y.-J. Liang, L. Wang, Y. Wen, et al., High-content ductile coherent nanoprecipitates achieve ultrastrong high-entropy alloys, Nat. Commun. 9 (1) (2018) 4063.
[3] T. Li, T. Liu, S. Zhao, et al., Ultra-strong tungsten refractory high-entropy alloy via stepwise controllable coherent nanoprecipitations, Nat. Commun. 14 (1) (2023) 3006.
[4] Z. Fu, L. Jiang, J.L. Wardini, et al., A high-entropy alloy with hierarchical nanoprecipitates and ultrahigh strength, Sci. Adv. 4 (10) (2018) eaat8712.
[5] K. Ming, X. Bi, J. Wang, Realizing strength-ductility combination of coarse-grained $Al_{0.2}Co_{1.5}CrFeNi_{1.5}Ti_{0.3}$ alloy via nano-sized, coherent precipitates, Int. J. Plast. 100 (2018) 177–191.
[6] E. Ma, C. Liu, Chemical inhomogeneities in high-entropy alloys help mitigate the strength-ductility trade-off, Prog. Mater. Sci. (2024) 101252.
[7] J. He, H. Wang, H. Huang, et al., A precipitation-hardened high-entropy alloy with outstanding tensile properties, Acta Mater. 102 (2016) 187–196.
[8] Y. Zhao, T. Yang, Y. Tong, et al., Heterogeneous precipitation behavior and stacking-fault-mediated deformation in a CoCrNi-based medium-entropy alloy, Acta Mater. 138 (2017) 72–82.

[9] S. Peng, Y. Wei, H. Gao, Nanoscale precipitates as sustainable dislocation sources for enhanced ductility and high strength, Proc. Natl. Acad. Sci. 117 (10) (2020) 5204–5209.
[10] D.-H. Lee, J.-A. Lee, Y. Zhao, et al., Annealing effect on plastic flow in nanocrystalline CoCrFeMnNi high-entropy alloy: a nanomechanical analysis, Acta Mater. 140 (2017) 443–451.
[11] H. Bei, Y.F. Gao, S. Shim, et al., Strength differences arising from homogeneous versus heterogeneous dislocation nucleation, Phys. Rev. B 77 (6) (2008) 060103.
[12] Y. Gao, H. Bei, Strength statistics of single crystals and metallic glasses under small stressed volumes, Prog. Mater. Sci. 82 (2016) 118–150.
[13] J.K. Mason, A.C. Lund, C.A. Schuh, Determining the activation energy and volume for the onset of plasticity during nanoindentation, Phys. Rev. B 73 (5) (2006) 054102.
[14] Y. Sato, S. Shinzato, T. Ohmura, et al., Unique universal scaling in nanoindentation pop-ins, Nat. Commun. 11 (1) (2020) 4177.
[15] A. Barnoush, Correlation between dislocation density and nanomechanical response during nanoindentation, Acta Mater. 60 (3) (2012) 1268–1277.
[16] Y. Zhao, J.M. Park, J.i. Jang, et al., Bimodality of incipient plastic strength in face-centered cubic high-entropy alloys, Acta Mater. 202 (2021) 124–134.
[17] K. Gan, D. Yan, S. Zhu, et al., Interstitial effects on the incipient plasticity and dislocation behavior of a metastable high-entropy alloy: nanoindentation experiments and statistical modeling, Acta Mater. 206 (2021) 116633.
[18] Q. Zhang, X. Jin, X.H. Shi, et al., Short range ordering and strengthening in CoCrNi medium-entropy alloy, Mater. Sci. Eng.: A 854 (2022) 143890.
[19] Q. Zhang, P.K. Liaw, H.J. Yang, et al., Short-range-ordering strengthening and the evolution of dislocation-nucleation modes in an $Fe_{40}Mn_{20}Cr_{20}Ni_{20}$ high-entropy alloy, Mater. Sci. Eng.: A 873 (2023) 145038.
[20] G. Yang, Y. Zhao, D.-H. Lee, et al., Influence of hydrogen on incipient plasticity in CoCrFeMnNi high-entropy alloy, Scr. Mater. 161 (2019) 23–27.
[21] C. Zhu, Z.P. Lu, T.G. Nieh, Incipient plasticity and dislocation nucleation of FeCoCrNiMn high-entropy alloy, Acta Mater. 61 (8) (2013) 2993–3001.
[22] C.A. Schuh, A.C. Lund, Application of nucleation theory to the rate dependence of incipient plasticity during nanoindentation, J. Mater. Res. 19 (7) (2004) 2152–2158.
[23] C.A. Schuh, J.K. Mason, A.C. Lund, Quantitative insight into dislocation nucleation from high-temperature nanoindentation experiments, Nat. Mater. 4 (8) (2005) 617–621.
[24] T. Rouxel, J.-i. Jang, U. Ramamurty, Indentation of glasses, Prog. Mater. Sci. 121 (2021).
[25] A.-H. Jeon, Y. Zhao, Z. Gao, et al., Stochastic nature of incipient plasticity in a body-centered cubic medium-entropy alloy, Acta Mater. 278 (2024) 120244.
[26] A. Montagne, V. Audurier, C. Tromas, Influence of pre-existing dislocations on the pop-in phenomenon during nanoindentation in MgO, Acta Mater. 61 (13) (2013) 4778–4786.
[27] T. Ohmura, L. Zhang, K. Sekido, et al., Effects of lattice defects on indentation-induced plasticity initiation behavior in metals, J. Mater. Res. 27 (13) (2012) 1742–1749.
[28] Y. Zhao, H. Chen, Z. Lu, et al., Thermal stability and coarsening of coherent particles in a precipitation-hardened $(NiCoFeCr)_{94}Ti_2Al_4$ high-entropy alloy, Acta Mater. 147 (2018) 184–194.
[29] G. Laplanche, S. Berglund, C. Reinhart, et al., Phase stability and kinetics of a sigma-phase precipitation in CrMnFeCoNi high-entropy alloys, Acta Mater. 161 (2018) 338–351.
[30] K.L. Johnson, Contact Mechanics, Cambridge University Press, Cambridge, 1985.
[31] A. Naghdi, F.J. Domínguez-Gutiérrez, W.Y. Huo, et al., Dynamic nanoindentation and short-range order in equiatomic NiCoCr medium-entropy alloy lead to novel density wave ordering, Phys. Rev. Lett. 132 (11) (2024) 116101.
[32] T.W. Clyne, J.E. Campbell, M. Burley, et al., Profilometry-based inverse finite element method indentation plastometry, Adv. Eng. Mater. 23 (9) (2021) 2100437.
[33] C.A. Schneider, W.S. Rasband, K.W. Eliceiri, NIH image to ImageJ: 25 years of image analysis, Nat. Methods 9 (7) (2012) 671–675.
[34] C.T. Rueden, J. Schindelin, M.C. Hiner, et al., ImageJ2: imageJ for the next generation of scientific image data, BMC. Bioinform. 18 (2017).
[35] P.W. Voorhees, The theory of Ostwald ripening, J. Stat. Phys. 38 (1985) 231–252.
[36] E. Marquis, D.N. Seidman, Nanoscale structural evolution of Al3Sc precipitates in Al (*Sc*) alloys, Acta Mater. 49 (11) (2001) 1909–1919.
[37] J. Zhang, L. Liu, T. Huang, et al., Coarsening kinetics of γ' precipitates in a re-containing Ni-based single crystal superalloy during long-term aging, J. Mater. Sci. Technol. 62 (2021) 1–10.
[38] J. Zhang, T. Huang, K. Cao, et al., A correlative multidimensional study of γ' precipitates with Ta addition in re-containing Ni-based single crystal superalloys, J. Mater. Sci. Technol. 75 (2021) 68–77.
[39] Y. Wu, C. Li, X. Xia, et al., Precipitate coarsening and its effects on the hot deformation behavior of the recently developed γ'-strengthened superalloys, J. Mater. Sci. Technol. 67 (2021) 95–104.
[40] Y. Zhao, I.-C. Choi, Y.-J. Kim, et al., On the nanomechanical characteristics of thermally-treated alloy 690: grain boundaries versus grain interior, J. Alloys. Compd. 582 (2014) 141–145.
[41] Y. Zhao, H. Chen, Z. Lu, et al., Thermal stability and coarsening of coherent particles in a precipitation-hardened $(NiCoFeCr)_{94}Ti_2Al_4$ high-entropy alloy, Acta Mater. 147 (2018) 184–194.
[42] P. Pandey, S. Kashyap, D. Palanisamy, et al., On the high temperature coarsening kinetics of γ' precipitates in a high strength $Co_{37.6}Ni_{35.4}Al_{9.9}Mo_{4.9}Cr_{5.9}Ta_{2.8}Ti_{3.5}$ fcc-based high entropy alloy, Acta Mater. 177 (2019) 82–95.
[43] D. Zhang, J. Kuang, H. Xue, et al., A strong and ductile NiCoCr-based medium-entropy alloy strengthened by coherent nanoparticles with superb thermal-stability, J. Mater. Sci. Technol. 132 (2023) 201–212.
[44] X. Bai, W. Fang, R. Chang, et al., Effect of Cr content on precipitation behavior of $(CoCrNi)_{94}Ti_3Al_3$ medium entropy alloys, Intermetallics. (Barking) 132 (2021) 107125.
[45] W. Lu, X. Luo, B. Huang, et al., Excellent thermal stability and their origins in γ' precipitation-strengthened medium-entropy alloys, Scr. Mater. 212 (2022) 114576.
[46] Y. Zhao, T. Yang, B. Han, et al., Exceptional nanostructure stability and its origins in the CoCrNi-based precipitation-strengthened medium-entropy alloy, Mater. Res. Lett. 7 (4) (2019) 152–158.
[47] J.H. Perepezko, S.D. Imhoff, M.-W. Chen, et al., Nucleation of shear bands in amorphous alloys, Proc. Natl. Acad. Sci. U.S.A. 111 (11) (2014) 3938–3942.
[48] S. Nag, R.L. Narayan, J.-i. Jang, et al., Statistical nature of the incipient plasticity in amorphous alloys, Scr. Mater. 187 (2020) 360–365.
[49] W. Abuzaid, H. Sehitoglu, Critical resolved shear stress for slip and twin nucleation in single crystalline FeNiCoCrMn high entropy alloy, Mater. Charact. 129 (2017) 288–299.
[50] N.L. Okamoto, S. Fujimoto, Y. Kambara, et al., Size effect, critical resolved shear stress, stacking fault energy, and solid solution strengthening in the CrMnFeCoNi high-entropy alloy, Sci. Rep. 6 (1) (2016) 35863.
[51] S. Mridha, M. Sadeghilaridjani, S. Mukherjee, Activation volume and energy for dislocation nucleation in multi-principal element alloys, Metals. (Basel) 9 (2) (2019) 263.
[52] Q. Zhang, X. Jin, H.J. Yang, et al., Gradient plastic zone model in equiatomic face-centered cubic alloys, J. Mater. Sci. 57 (46) (2022) 21475–21490.
[53] Z. Wang, C. Liu, P. Dou, Thermodynamics of vacancies and clusters in high-entropy alloys, Phys. Rev. Mater. 1 (4) (2017) 043601.
[54] W. Chen, X. Ding, Y. Feng, et al., Vacancy formation enthalpies of high-entropy FeCoCrNi alloy via first-principles calculations and possible implications to its superior radiation tolerance, J. Mater. Sci. Technol. 34 (2) (2018) 355–364.
[55] C. Li, J. Yin, K. Odbadrakh, et al., First principle study of magnetism and vacancy energetics in a near equimolar NiFeMnCr high entropy alloy, J. Appl. Phys. 125 (15) (2019).
[56] K. Sugita, N. Matsuoka, M. Mizuno, et al., Vacancy formation enthalpy in CoCrFeMnNi high-entropy alloy, Scr. Mater. 176 (2020) 32–35.
[57] Y. Zhang, A. Manzoor, C. Jiang, et al., A statistical approach for atomistic calculations of vacancy formation energy and chemical potentials in concentrated solid-solution alloys, Comput. Mater. Sci. 190 (2021) 110308.
[58] N. Hiroshi, Defects in Metals, Physical Metallurgy, Elsevier, 2014, pp. 561–637.
[59] D. Lorenz, A. Zeckzer, U. Hilpert, et al., Pop-in effect as homogeneous nucleation of dislocations during nanoindentation, Phys. Rev. B 67 (17) (2003) 172101.
[60] S. Shim, H. Bei, E.P. George, et al., A different type of indentation size effect, Scr. Mater. 59 (10) (2008) 1095–1098.
[61] L. Wang, Y. Cao, Y. Zhao, Lattice distortion promotes incipient plasticity in multiprincipal element alloys, Nano Lett. 24 (29) (2024) 9004–9010.
[62] A. Chauniyal, R. Janisch, How coherent and semi-coherent interfaces govern dislocation nucleation in lamellar TiAl alloys, Adv. Eng. Mater. 25 (15) (2023) 2300121.
[63] Y. Ou, Y. Jiang, Y. Wang, et al., Vacancy and solute co-segregated η_1 interface in over-aged Al-Zn-Mg alloys, Acta Mater. 218 (2021) 117082.
[64] Q.J. Li, H. Sheng, E. Ma, Strengthening in multi-principal element alloys with local-chemical-order roughened dislocation pathways, Nat. Commun. 10 (1) (2019).
[65] C. Schuh, T. Nieh, H. Iwasaki, The effect of solid solution W additions on the mechanical properties of nanocrystalline Ni, Acta Mater. 51 (2) (2003) 431–443.
[66] J. He, W. Liu, H. Wang, et al., Effects of Al addition on structural evolution and tensile properties of the FeCoNiCrMn high-entropy alloy system, Acta Mater. 62 (2014) 105–113.
[67] M. Phillips, B. Clemens, W. Nix, A model for dislocation behavior during deformation of Al/Al3Sc (fcc/$L1_2$) metallic multilayers, Acta Mater. 51 (11) (2003) 3157–3170.
[68] F. Siska, T. Guo, L. Stratil, et al., Numerical study of stress distribution and size effect during AZ31 nanoindentation, Comput. Mater. Sci. 126 (2017) 393–399.
[69] K. Durst, B. Backes, M. Goken, Indentation size effect in metallic materials: correcting for the size of the plastic zone, Scr. Mater. 52 (11) (2005) 1093–1097.
[70] K. Durst, B. Backes, O. Franke, et al., Indentation size effect in metallic materials: modeling strength from pop-in to macroscopic hardness using geometrically necessary dislocations, Acta Mater. 54 (9) (2006) 2547–2555.
[71] T. Ohmura, M. Wakeda, Pop-in phenomenon as a fundamental plasticity probed by nanoindentation technique, Materials. (Basel) 14 (8) (2021) 1879.